

## Supplementary Information for “Rapid Capillary Filling via Ion-Water Interactions over Nanoscale”

Chirodeep Bakli and Suman Chakraborty\*

Department of Mechanical Engineering, Indian Institute of Technology Kharagpur,  
Kharagpur 721302, INDIA

### Simulation Details

A slit of height 1.5 nm is connected to a reservoir having dimension of 12×12×10 nm. The reservoir walls are constituted of particles in FCC lattice. The slit, which runs across the width of the reservoir, is mimicked to be etched out of a crystal having FCC lattice in <100> plane. The slit walls are thick and atomically smooth. The reservoir is large enough to sustain the capillarity while water imbibes into the slit. Periodic boundary conditions are applied in the plane of the reservoir, rationalizing the treatment of water in the reservoir as bulk fluid. The dimensions of the reservoir and thus the number of water molecules in it are much larger as compared to the slit. This ensures that the water in the reservoir is always in equilibrium with its vapor and a constant pressure is maintained in the reservoir during the entire imbibition period. The initial density of water inside the reservoir is based on the density of water at 300K and hence, the reservoir, in this case, accommodates 48204 water molecules.

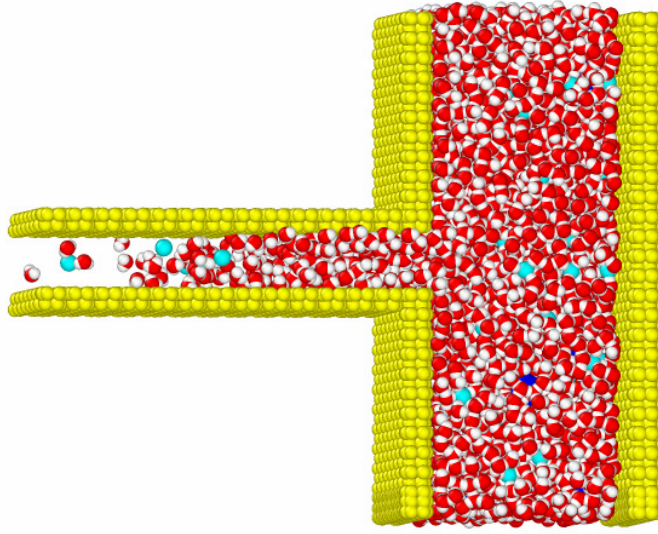


**Figure S1.** An explored view of the simulation domain. Reservoir containing water with dissolved NaCl is connected to the slit into which the fluid imbibes. The cyan particles are  $\text{Na}^+$  ions and blue (particles are Cl ions).

In order to simulate saline solutions, sodium and chloride ions are randomly distributed in the fluid bulk. The number of ions is determined from the molarity of the solution being simulated, which, for the present study, has been varied from  $0.1\text{ M} - 2\text{ M}$ . The formation of electrical double layer (EDL) is accounted for by assigning a uniformly distributed negative charge on the wall particles in contact with the fluid and maintaining the electro-neutrality by having less number of anions than cations. In order to segregate the effect of electrostatics and hydrodynamics, we simulated the same geometrical system with varying fixed charge and random free charge configurations. Based on the theory of development of EDL following ion adsorption and de-protonation on interaction of the saline solution with the surface, this model is physically quite realistic<sup>1</sup>. A more realistic mode natural charge acquisition of solid surfaces, however, would be through charged groups at the surface. To mimic the same, we assigned a unit of electronic charge ( $e$ ) to random wall atoms summing up to the desired surface charge density intended for the total wall. We repeated the simulation with random distribution of this discrete surface charge on the wall. The slip data obtained for all the above combinations was

used to obtain the slip length variation which was further used in the analysis. The slip length values lie within the errorbar regime as shown in the figures and given the thermal fluctuations. Thus, we conclude that the charge distribution does not introduce any artifact to the simulation results. This observation is in concordance with the existing literature<sup>2,3</sup>.

The simple point charge/extended (SPC/E)<sup>4</sup> model for water is used, which captures with accuracy the hydrodynamic and the electrostatic interactions in the fluid and at the same time optimizes the computation time. The walls are modeled as Lennard-Jones (LJ) particles which interact with the ions and water by van der Waals interactions. The charges on the wall particles, the ions and the dipoles on water molecules contribute to electrostatic interaction. The wall atoms are allowed to vibrate about their equilibrium positions instead of being rigid. This corresponds to a more physically realistic situation and removes the artifacts that may be incurred due to fixed walls<sup>5</sup>. The wall atoms are tethered to springs of sufficiently high spring constants so as to prevent vibrations over a threshold level<sup>6</sup>. The walls are thermostatted using Nosé-Hoover thermostat at 300K and the fluid molecules are allowed to exchange heat via collisions with the flexible wall and hence maintain the temperature.

With the initial velocities determined using Maxwellian distribution at 300K, the saline solution is energy minimized and equilibrated. The trajectories of the particles are obtained by integration using leap-frog algorithm over time. A typical simulation runs for 5ns ( $5 \times 10^6$  time steps). We use size of time step to be 0.001 ps. 50 independent simulation runs, starting from different random initial distributions, are performed and the results are averaged to obtain robust and reproducible output.<sup>7</sup>

The intrinsic wettability of the surface is varied by tuning the LJ parameters of the wall atoms which alters the van der Waals interactions between the wall and the water molecules. The homo-nuclear LJ parameters of the wall particles  $\epsilon_{ww}$  ranges from 2.5 kJ / mol to 6 kJ / mol, and  $\sigma_{ww} = 0.35nm$  is kept fixed for the simulations. The homo-nuclear interaction parameters are shown in table 1. The hetero-nuclear LJ interactions are obtained using standard mixing rules<sup>8</sup>. This gives an effective variation of the contact angle from  $0^\circ - 70^\circ$  benchmarked for a sessile droplet on a geometrically similar surface having the same set of potential parameters. A droplet comprising 1331 water molecules is arranged in a cubic lattice and allowed to spread over a

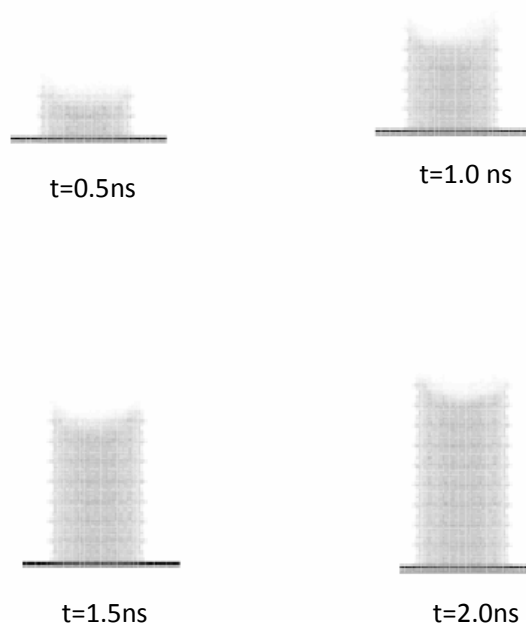
surface constructed using particles in FCC lattice in  $\langle 100 \rangle$  plane. In order to obtain saline solutions, ions are randomly placed within the water droplet. The number of ions is determined by the molarity of the saline solution which is varied from  $0.1M - 2.0M$ . The substrate acquires charge in contact with a polar fluid like water. The total fixed surface charge together with the free charge or the imbalance in the anionic and cationic charge ensure overall electroneutrality. The droplet is equilibrated over the surface for a simulation run of 20 ns. It is observed that this time has sufficient allowance for the droplet to reach equilibrium and no further evolution of droplet shape occurs. Following this, the droplet is binned. From the number density of water molecules in each of the bins, the droplet profile and hence, the contact angle is obtained. We repeat the simulations for a film of water on a substrate allowed to aggregate and form a droplet as guided by the substrate wettability. The results obtain from film aggregation simulation tally with the results of droplet spreading.

Table 1. Homonuclear interaction potentials

<b>Particles</b>	<b><math>\sigma</math> (nm)</b>	<b><math>\epsilon</math> (kJ/mol)</b>
<b>Oxygen</b>	<b>0.3167</b>	<b>0.650</b>
<b>Wall</b>	<b>0.350</b>	<b>2.5-6</b>
<b>Na+</b>	<b>0.257</b>	<b>0.063</b>
<b>Cl-</b>	<b>0.445</b>	<b>0.444</b>

The electrostatic interactions are accounted for using a particle-particle particle-mesh (PPPM) algorithm. For the simulations, we have chosen a van der Waals cut-off distance of  $5\sigma_{ww}$ . In order to determine the filling rates and the exact location of the meniscus, the slit is divided into bins of optimum size so as to obtain the appropriate curvature shape without encountering abrupt density fluctuations in the resulting profile. The number density of the water molecules is obtained in the bins averaged over the slit width. A sharp transition in the number density indicates the temporal location of the meniscus<sup>9</sup>. The dynamic evolution of the meniscus position is observed by tracking the density distribution in these bins. We do not attempt to

analyze the dynamic contact angle of the meniscus, as the imbibing meniscus does not retain a perfect concave shape throughout, due to the action of electrostatic forces on the interface in presence of surface charges and ions. This idea can be perceived graphically from the number density snapshots represented in terms of pixels in the slit pore at various time instances in fig. S2. We track numerically this drop in number density and track the loci of such points to obtain meniscus position.



**Figure S2.** Number density diagrams for water molecules in the slit at different time intervals. The temporal position of the meniscus can be tracked from the density variation of water molecules in the pore.

## Theory

The balance of forces in a charged slit of height  $2H$  and width  $W$  can be written as:

$$\frac{d}{dt}(Mu) = F_{vis} + F_e + F_{lap} \quad (1)$$

The instantaneous force balance equation includes the force due to the Laplace pressure gradient ( $F_{lap}$ ) across the meniscus, a retarding viscous drag ( $F_{vis}$ ) due to the motion of the liquid column, and the electrical force ( $F_e$ ) under the action of the streaming potential on the charged species in the capillary. One may note here that the inertia term  $\frac{d}{dt}(Mu)$ : with  $M$  as the instantaneous mass of the liquid column and  $u$  as the instantaneous velocity of the centre of mass of the liquid in the capillary, may be neglected for nanoscale capillary filling, without sacrificing the essential physics of interest<sup>10,11</sup>.

Expressions for the various forces in Eq. (1) are as follows. The capillary force is given by

$$F_{lap} = 2(W + 2H) \gamma \cos \theta \quad (2)$$

where  $\gamma$  is the fluid-vapor surface tension at the air-water interface, and  $\theta$  is the contact angle.  $F_e = q_p E_s$  is the electrical force on the meniscus, with  $q_p$  being the net charge in the solution contributed by the dissolved ionic species and  $E_s$  is the streaming potential field.

The electrical force would depend on the charge distribution within the electrical double layer (EDL), which, in turn, is related to the EDL potential  $\psi$ . The later can be obtained from the Poisson-Boltzmann equation<sup>1</sup>, corresponding to a  $z$ :  $z$  symmetric electrolyte, as

$$\frac{d}{dy} \left( \epsilon \frac{d\psi}{dy} \right) = 2ze n_o \sinh \left( \frac{ze\psi}{k_B T} \right) \quad (3)$$

In the above equation,  $y$  is the wall-normal coordinate,  $e$  is the protonic charge,  $z$  is the valance of ion,  $k_b$  is the Boltzmann constant,  $T$  is the absolute temperature, and  $n_o$  is the ion density in

the bulk. Eq. (3) is essentially the Poisson equation, supplemented by the Boltzmann distribution of the ionic species:  $n_{\pm} = n_o \exp\left(\mp \frac{ze\psi}{k_B T}\right)$ , where  $n_+$  and  $n_-$  are the cationic and anionic number densities, respectively. The free charge within the fluid in the slit at any time instant, thus, can be expressed as

$$q_p = L \int_{-H}^H ze(n_+ - n_-)Wdy = -\frac{4n_o WLz^2 e^2 \zeta \lambda}{k_B T} \tanh(H/\lambda) \quad (4)$$

Here  $\zeta$  is the zeta potential of the surface and  $\lambda$  is the Debye length given by the expression:

$$\lambda = \sqrt{\frac{\epsilon k_B T}{2n_o e^2 z^2}} \quad 1,12.$$

A further simplified expression for  $q_p$  may be obtained by assuming Debye-Hückel

linearization<sup>1</sup> for low zeta potentials, so that:  $\sinh\left(\frac{ze\psi}{k_B T}\right) = \frac{ze\psi}{k_B T}$ .

The viscous force can be expressed in terms of the cross-gradient of the fluid velocity within the slit:  $F_{vis} = 2(W + 2H)\eta L(\partial u/\partial y)_{y=\pm H}$ ,  $\eta$  being the viscosity of the liquid. For all calculations, we consider  $W \gg H$ . The flow within the slit occurs under the combined action of force due to the Laplace pressure gradient and the electrical force, and thus, the resulting velocity profile would be a linear superposition of the pressure driven and electrokinetic components, so that

$$u = u_p + u_e \quad (5)$$

Here  $u_p$  and  $u_e$  are the pressure driven and electrokinetic velocity components, respectively. The comparable, bulk and interfacial scales makes it imperative to consider fluid slip at the boundaries, and thus, the velocity profiles can be expressed as:

$$\begin{aligned}
u_p &= \left( \frac{\gamma \cos \theta}{HL} \right) \left[ \frac{(H^2 - y^2)}{2\eta} + \frac{(l_{sp}/H)}{\eta} H^2 \right] \\
u_e &= \left( \frac{\varepsilon E_s \zeta}{\eta} \right) \left[ \frac{\cosh(y/\lambda)}{\cosh(H/\lambda)} - 1 + \frac{l_{se}}{\lambda} \tanh(H/\lambda) \right]
\end{aligned} \tag{6}$$

In Eq. (6),  $\gamma \cos \theta / HL$  is the Laplace pressure gradient for an instantaneous capillary penetration depth of  $L$ . Further,  $l_{sp}$  and  $l_{se}$  are the Navier slip lengths for the pressure-driven and electrokinetic velocity components, respectively.

The average velocity in the slit  $\langle u \rangle$  may be expressed as

$$\langle u \rangle = \frac{\int_{-H}^H W(u_p + u_e) dy}{\int_{-H}^H W dy} = \langle u_p \rangle + \langle u_e \rangle \tag{7}$$

where  $\langle u_p \rangle$  and  $\langle u_e \rangle$  are the average velocity contributions from pressure driven and electrokinetic flows respectively, and are expressed as

$$\begin{aligned}
\langle u_p \rangle &= \frac{H^2}{3\eta} \left( \frac{\gamma \cos \theta}{HL} \right) \left( 1 + \frac{3l_{sp}}{H} \right) \\
\langle u_e \rangle &= \left( \frac{\varepsilon E_s \zeta}{\eta} \right) \left[ \left( \frac{\lambda}{H} + \frac{l_{se}}{\lambda} \right) \tanh(H/\lambda) - 1 \right]
\end{aligned} \tag{8}$$

Letting  $\frac{\langle u_e \rangle}{\langle u_p \rangle} = R$ , one may express the wall-normal velocity gradient as:

$$\left. \frac{\partial u}{\partial y} \right|_{y=\pm H} = \langle u \rangle \left\{ \left( \frac{-3}{(1+R)(H+l_{sp})} \right) + \frac{R}{\lambda(1+R)} \frac{\tanh(H/\lambda)}{\left( \frac{\lambda}{H} + \frac{l_{se}}{\lambda} \right) \tanh(H/\lambda) - 1} \right\} \tag{9}$$

Thus, the resistive viscous force in Eq. (1) becomes:

$$F_{vis} = 2(W + 2H)\eta L \langle u \rangle \left\{ \left( \frac{-3}{(1+R)(H+l_{sp})} \right) + \frac{R}{\lambda(1+R)} \frac{\tanh(H/\lambda)}{\left( \frac{\lambda}{H} + \frac{l_{se}}{\lambda} \right) \tanh(H/\lambda) - 1} \right\} \quad (10)$$

The balance of forces expressed by Eq. (1) remains yet to be mathematically closed, because of an unknown parameter  $E_s$  (dynamically evolving induced axial potential gradient across the meniscus) involved with the expressions for the electrokinetic and the viscous forces. In an effort to achieve a closure to this problem, we first express the ionic velocities as a sum of the advective and electromigrative velocity components, so that

$$u_{\pm} = u_p + u_e \pm \frac{zeE_s}{f} \quad (11)$$

Here  $f$  is the ionic friction factor, expressed in terms of ionic diffusivity,  $D$ , as  $f = k_B T / D$ . Accordingly, one may evaluate the net ionic current through each section of the channel. In the absence of any externally applied axial electric field (as in the present case), the net ionic current through each section must be zero. Accordingly, one may write:

$$ze \int_{-H}^H (n_+ u_+ - n_- u_-) W dy = 0 \quad (12)$$

Substituting the expressions for  $u_p$ ,  $u_e$ ,  $n_{\pm}$  in Eq. (12), one may finally obtain

$$E_s = \frac{\frac{\zeta \gamma \lambda^2}{\eta L} \cos \theta \left( \frac{\lambda}{H} \tanh(H/\lambda) - 1 \right) - \zeta u_s \lambda \tanh(H/\lambda)}{\frac{k_B T H}{f} + \frac{\epsilon \zeta^2}{2\eta} \left( \lambda \tanh(H/\lambda) - \frac{H}{(\cosh(H/\lambda))^2} \right)} \quad (13)$$

The electrical force acting on the capillary can now be expressed as  $F_e = q_p E_s$ , where  $q_p$  may be expressed using Eq. (4) and  $E_s$  is described by Eq. (13). Accordingly:

$$F_e = \left[ \frac{\frac{\zeta \lambda^2}{\eta L} \cos \theta \left( \frac{\lambda}{H} \tanh \left( \frac{H}{\lambda} \right) - 1 - \frac{l_{sp}}{\lambda} \tanh \left( \frac{H}{\lambda} \right) \right)}{\frac{k_B T H}{f} + \frac{\epsilon \zeta^2}{2\eta} \left( \lambda \tanh \left( \frac{H}{\lambda} \right) - \frac{H}{\cosh^2 \left( \frac{H}{\lambda} \right)} + 2l_{se} \tanh^2 \left( \frac{H}{\lambda} \right) \right)} \right] \left[ -\frac{4n_o W L z^2 e^2 \zeta \lambda}{k_B T} \tanh \left( \frac{H}{\lambda} \right) \right] \quad (14)$$

The balance of capillary, viscous and electrical forces can be utilized to obtain the dynamical evolution of the capillary meniscus. However, for a successful implementation of the same, one need to incorporate appropriate values of the slip lengths in the calculation, which may be obtained from the MD simulation data, as a combined function of the intrinsic wettability, surface charge, and salt concentration.

### Variation of slip length with contact angle, salt concentration and surface charge

Since the magnitude of the velocity jump can depend on the flow actuating mechanism, the pressure gradient driven flow and electrokinetically driven flows have different interfacial characteristics and hence different viscous shear stresses. To discern the effect of flow actuating mechanism on the slip length, we propose two artificial slip lengths individually accounting for sole electrokinetic flow component and the pressure gradient component. The net interfacial velocity is the sum total of the pressure-driven and electrokinetic velocity components, so that one may write

$$u_s = u_{sp} + u_{se}$$

$$l_s \frac{\partial u}{\partial y} = l_{sp} \frac{\partial u_p}{\partial y} + l_{se} \frac{\partial u_e}{\partial y}$$

We perform independent non-equilibrium simulations in completely filled channels varying salt concentration, wettability and surface charge density to determine the slip length parameters. Obtaining  $l_{sp}$  or the slip length due to sole contribution of pressure gradient is straight forward. We simulate a Poiseuille flow using a body force for actuation mimicking pressure gradient. The

velocity profile obtained from extrapolating the molecular flow profile is expressed in terms of Navier boundary conditions to obtain the slip length. On the same simulation domain, we introduce ions and surface charge and thus introducing electrokinetic effects. Introduction of charges would alter the flow characteristics and would more drastically modify the flow in the interfacial region. Now, we can expect the velocity profile to be a superposition of the electrokinetic and pressure driven component. Derivation of slip length from this flow profile yields the combined slip length  $l_s$  and  $l_{se}$  can be obtained from the above equation. It must be noted that  $l_{se}$  is an artificial parameter used to indicate the contribution of electrostatics toward slip. For the cases of wettability and salt concentration variation, the surface charge density is kept constant at  $0.024\text{C/m}^2$ . Figures S3 and S4 show the effect of wettability and salt concentration on slip length respectively.

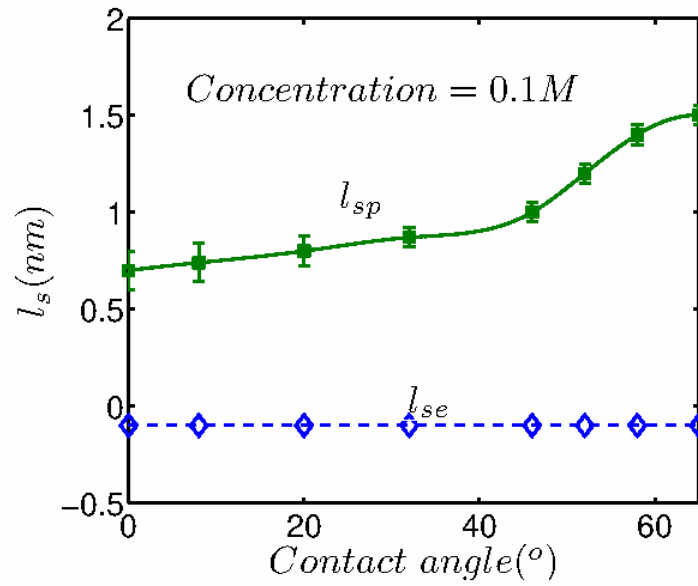


**Figure S3.** Variation of electrokinetic and pressure driven components of slip length with surface wettability for a saline solution having concentration of 0.1M. Electrokinetic slip length, by definition, does not vary with wettability, and is shown by dashed line. The pressure driven flow component of slip from the simulation is shown with errorbar and the solid line is a guide to the eye.

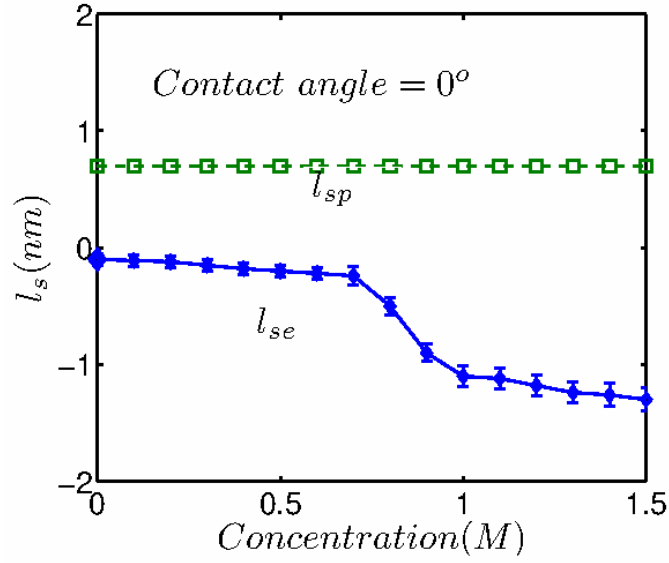


**Figure S4.** Variation of electrokinetic and pressure driven components of slip length with salt concentration for a completely wettable channel. The pressure driven component of slip length, by definition, does not vary with salt concentration. The electrokinetic component of slip from the simulation is shown with errorbar and the solid line is a guide to the eye.

In the case of variation of surface charge density, the ratio of free charge and fixed charge in the system is kept constant, to obtain slip lengths for a constant Dukhin number. Fig. S5 shows the variation of slip length with surface charge parameter. Considering surface charge to alter only the electrostatic interactions, as embedded in the definition of  $l_{se}$ , we can compare our slip length variation with the existing literature which considers such electrostatic effects modulating slip. The trend in slip length variation agrees with the results of Joly et al.<sup>13</sup>

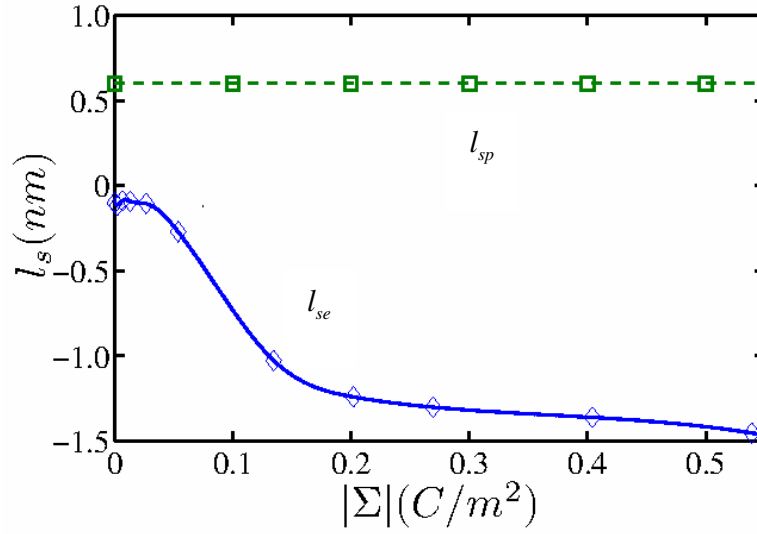


**Figure S5.** Variation of electrokinetic and pressure driven components of slip length with surface charge density for a completely wettable channel.

### Amplification of filling rates in moderately wettable channels

The filling rate in partially filling pores increase by around 10% than that of completely filling pores. This occurs due to alteration of the polarizability of the interfacial fluid which tunes the van der Waals forces making partially wettable pores effectively more wettable. However, if the filling rate in a partially wettable pore (say 46°) is compared with the LW analysis after imposing theoretical electroviscous retardation, an increase of 40-50% is observed. This relative enhancement of filling rate is captured in fig. S6.

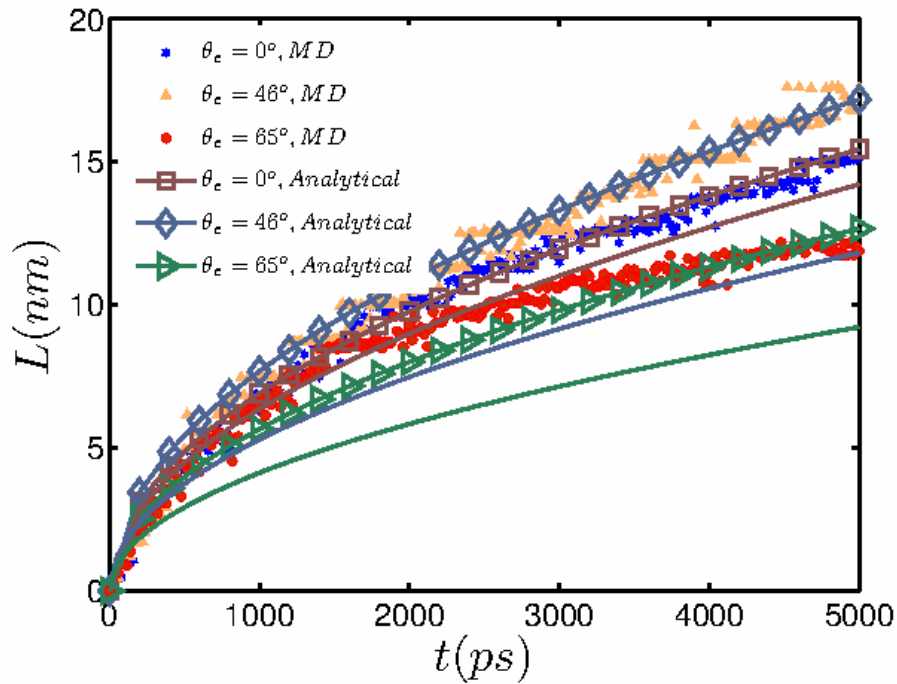


**Figure S6.** The instantaneous filling lengths of capillaries with varying wettabilities at high salt concentration (1.5 M). Completely wettable pores do not show the maximum filling speeds. The driving surface tension force decreases with wettability and so does the viscous force. However, the opposing electrokinetic force shows a greater decrease leading to rapid filling in partially wettable pores, as compared to completely wettable ones. The bold lines indicate the filling rates of capillaries obtained from theoretical Lucas Washburn (LW) model with electroviscous retardation. The blue bold line and blue diamond markers indicate 40-50% faster filling in moderately hydrophilic (contact angle  $46^\circ$ ) charged capillaries as observed in simulations and predicted by our model as compared to the classical theoretical model<sup>14,15</sup>.

## REFERENCES

1. R. J. Hunter, *Zeta Potential in Colloid Science: Principles*, Academic Press, 1981.
2. D. Ben-Yaakov, D. Andelman, and H. Diamant, *Phys. Rev. E. Stat. Nonlin. Soft Matter Phys.*, 2013, **87**, 022402.

3. F. Jiménez-Ángeles, *Phys. Rev. E. Stat. Nonlin. Soft Matter Phys.*, 2012, **86**, 021601.
4. H. J. C. Berendsen, J. R. Grigera, and T. P. Straatsma, *J. Phys. Chem.*, 1987, **91**, 6269–6271.
5. A. Martini, H. Hsu, N. A. Patankar, and S. Lichter, *Phys. Rev. Lett.*, 2008, **206001**, 1–4.
6. P. P. A. Thompson and M. M. O. Robbins, *Phys. Rev. Lett.*, 1989, **63**, 766–769.
7. L. Makkonen, *Langmuir*, 2014.
8. M. P. Allen and D. J. Tildesley, *Computer Simulation of Fluids*, Clarendon Press, 1987.
9. G. Martic, T. D. Blake, J. De Coninck, and J. D. Coninck, *Langmuir*, 2005, **21**, 11201–11205.
10. R. Lucas, *Kolloid-Zeitschrift*, 1918, **23**, 15–22.
11. E. W. Washburn, *Phys. Rev.*, 1921, **17**, 391–283.
12. R.F. Probstein, *Physicochemical Hydrodynamics: An Introduction*, Wiley-Interscience, New York, 1994.
13. L. Joly, C. Ybert, E. Trizac, and L. Bocquet, *J. Chem. Phys.*, 2006, **125**, 204716.
14. S. Das, S. Chanda, J. C. T. Eijkel, N. R. Tas, S. Chakraborty, and S. K. Mitra, *Phys. Rev. E*, 2014, **90**, 043011.
15. V.-N. Phan, C. Yang, and N.-T. Nguyen, *Microfluid. Nanofluidics*, 2009, **7**, 519–530.